RSC Advances

ROYAL SOCIETY OF CHEMISTRY

www.rsc.org/advances

Self-assembled ultra-small zinc stannate nanocrystals with mesoscopic voids via salicylate templating pathway and their photocatalytic properties

Vandana Kumari, Astam K. Patra and Asim Bhaumik*

Department of Materials Science, Indian Association for the Cultivation of Science, Jadavpur, Kolkata - 700 032, India

*Address for correspondence. E-mail: msab@iacs.res.in

Abstract

Self-assembled tiny zinc stannate nanocrystals having controlled crystalline phases of $ZnSnO_3$ (MZS-1) and Zn_2SnO_4 (MZS-2) together with mesoscopic void spaces have been synthesized via salicylate templating method with particle dimensions of *ca.* 1-2 nm and 17-20 nm for MZS-1 and 2, respectively. These nanomaterials have been thoroughly characterized by powder XRD, HR TEM, N_2-sorption, TG-DTA and UV-Visible spectroscopic tools. Self-aggregation of the tiny nanoparticles could be responsible for these interparticle mesopores in these zinc stannate nanocrystals. Zn_2SnO_4 nanomaterial showed higher photocatalytic activity over that of $ZnSnO_3$ in the photodegradation of Rhodamine B under the irradiation of UV/visible light.

Introduction

Design and successful synthesis of ultra small semiconductor nanocrystals with controlled shape, size and their organized nanostructures through bottom-up chemistry approaches have long been an intensive and interdisciplinary area of research.[1] Along with quantum size effects, surface effects attain greater significance when the size of the nanocrystals is decreased to few nanometers because this resulted in rapid increase in the surface to volume ratio. Convenient syntheses of the nanocrystals through different synthetic and physical routes,[2]

large diversity in chemical compositions and novel properties of these nanocrystals have made them extremely active area of research for over last two decades, especially in optoelectronics,[3] sensing,[4] biomolecular separation,[5] drug delivery[6] and photocatalysis.[7] Often the self-assembly of these nanoparticles could be achieved in the presence of small functional organic molecules or templates, which could acts as the capping agent to stabilize the particular nanostructures.[8] This capping agent plays crucial role in directing the organized nanostructures through the self-aggregation of superstructures in solution phase.[9] Although, there are several strategies known for designing the self-assembled metal oxide nanoparticles,[10] synthesis of highly crystalline and tiny binary semiconducting mixed metal oxide nanocrystals together with nanoscale porosity is still a big challenge today.

Recently, researchers have focused a great deal of attention for the synthesis of self-assembled nanoparticles of CeO_2,[11] ZrO_2,[12] SnO_2,[13] Fe_3O_4,[14] ZnO,[15] etc. having interparticle voids. There are few reports of on the synthesis of $ZnSnO_3$ and Zn_2SnO_4 nanoparticles and their gas-sensing and photocatalytic properties.[16,17] Fan et al. have synthesized nanocrystalline hollow $ZnSnO_3$ microspheres by hydrothermal method, which showed good sensing for hydrocarbons like butane.[18] Self-assembly through non-covalent interactions, like H-bonding interaction,[19] π—π interaction,[20] etc. is one of the versatile techniques for the synthesis of different ultra-small nanostructured materials. Zhou et al have synthesized very small TiO_2 nanoparticles in room-temperature and these nanoparticles are self-assembled toward mesoporous spherical aggregates in presence of ionic liquid.[21] Oxide based nanomaterials having particle size ranging 1-10 nm can absorb larger number of photons at their surface due higher surface-to-volume ratio and quantum size effects vis-à-vis corresponding bulk materials.[22] Thus, to design the self-assembled zinc stannate nanoparticles with controllable particle size and interparticle void space using a

suitable capping agent is challenging as it can open new opportunities in optoelectronics,[23] and environmental remediation via photocatalysis.[24]

Environmental pollution caused by industrial effluents is one of the major concerns to our life today. Textile and other related chemical industries release several organic dyes and this is one of the major reasons for water pollution.[25] Thus, photocatalytic degradation of water pollutant organic dyes over porous zinc stannate nanomaterials can provide new insight to the existing dye degradation strategy.[26] Herein, we report the self-assembly of very tiny zinc stannate nanocrystals with mesoscopic void space via salicylate templating method depending upon various synthesis conditions. Particle size, surface area and related surface properties associated with the nanostructure plays crucial role in optical and photocatalytic performance of these materials. These nanomaterials have been characterized thoroughly and their catalytic role in the photodegradation of organic dyes in the presence of visible and UV light have been explored.

Experimental Section:

Chemicals:

Sodium salicylate (GR 99.5%, used as the structure-directing agent, anhydrous zinc chloride (98%) and diethylamine (99.5%, used to maintain the pH of the synthesis gel) were purchased from Merck, India. Tin chloride pentahydrate (98%) was obtained from Loba Chemie, India. All chemicals were used without any further purification.

Hydrothermal synthesis of zinc stannate ($ZnSnO_3$ and Zn_2SnO_4) nanoparticles:

Zinc stannate ($ZnSnO_3$ and Zn_2SnO_4) nanomaterials were synthesized via hydrothermal route by using sodium salicylate as a template. In a typical synthesis 1.6 g (0.01 mol) of sodium

salicylate was dissolved into 20 ml distilled water and 1 ml of diethylamine was added to this solution. Then the resultant solution was stirred for 30 min. Then 0.525 g (0.0038 mol) of the Zn(II) precursor, anhydrous $ZnCl_2$ and 0.675 g (0.0019 mol) of the Sn precursor, $SnCl_4.5H_2O$ was dissolved into 5 ml of distilled water separately and mixed together under stirring condition. The synthesis gel was prepared by adding the former template solution to the mixture of the acidic metal salt solution and the pH of the solution was raised up to 6.0 by adding additional diethylamine. Then the reaction mixture was stirred for 3 h and transferred in to a Teflon-lined stainless steel autoclave and hydrothermally treated at different temperatures, at 348, 373, 393, 423 and 448 K for 48 h. After the reaction, the autoclaves were cooled down to room temperature. The solids were collected through filtration, washed with deionized water for 3 times to remove the residual contaminant ions from the products and dried at room temperature. The sample synthesized at 348 K is designated as MZS-1 and that collected through hydrothermal treatment at 448 K followed by calcination at 773 K is abbreviated as MZS-2.

Characterization techniques:

Powder X-ray diffraction patterns of both as-synthesized and calcined samples were recorded on a Bruker D8 Advance SWAX diffractometer operated at 40 kV voltages and 40 mA current. The instrument has been calibrated with a standard silicon sample, using Ni-filtered Cu K_α (λ = 0.15406 nm) radiation. JEOL JEM 2010 transmission electron microscope operated at an accelerating voltage ranging from 100 kV to 200 kV has been employed for the determination of nanostructure and pore size. Nitrogen adsorption/desorption isotherms were obtained by using a Quantachrome Autosorb 1C surface area analyzer at 77 K. Prior to gas adsorption, samples were degassed for 4 h at 393 K under high vacuum. Thermogravimetric (TGA) and differential thermal analysis (DTA) of the samples were carried out in a TA Instruments thermal analyzer

TA-SDT Q-600 under air flow. FT IR spectra of the samples were recorded using a Nicolet MAGNA FT IR 750 spectrometer Series II. UV–visible diffuse reflectance spectra were recorded on a Shimadzu UV 2401PC coupled with an integrating sphere attachment. $BaSO_4$ was used as background standard.

Photocatalysis

The photocatalytic activity of porous zinc stannate ($ZnSnO_3$ and Zn_2SnO_4) nanomaterials was studied in the photodegradation of Rhodamine B by using different concentrations of dye solution in water (20 mg/L, 10 mg/L and 5 mg/L). Photodegradation kinetics was carried out with a photocatalytic reactor system in the presence of both UV (wavelength 250-390 nm) as well as under visible light (400 to 800 nm) irradiation. For UV source A 450 W medium-pressure Hg-vapor lamp (Hanovia) was placed inside the quartz tube. The lamp and the tube were immersed in the photoreactor cell, which is made up of Pyrex-glass. The temperature of the whole reactor was maintained at 298 K by using cold-water circulation to control the heat generated from the mercury-vapor lamp. The suspension was prepared by using 0.05 g photocatalyst in 10 mL dye solution (of different concentrations like 20 mgL^{-1}, 10 mgL^{-1} and 5 mgL^{-1}). Before photoirradiation, with either visible or UV light, the reactant solution with catalyst was stirred for 20 min in dark to establish the adsorption/desorption equilibrium. The reactant solution were placed under light irradiation in reactor and stirred magnetically to keep the suspension homogeneous. Then, at regular interval of times (20 min) about 1 mL of the reactant solution was withdrawn and centrifuged to remove the catalyst. The residual dye concentration was calculated from the absorbance values measured at 553 nm using the UV 2401PC UV–Visible spectrophotometer in solution phase.

Results and discussion:

Powder X-ray diffraction

The small angle powder X-ray diffraction pattern of as-synthesized MZS-1 is shown in Figure 1. A single broad peak for the mesophase with the peak maximum at $2\theta = 1.48^{o}$ could be attributed to the self-assembly of zinc stannate nanoparticles.[27] The average distance between the nanoparticles corresponding to this small angle diffraction is 5.9 nm, which suggests that MZS-1 is composed of very tiny self-assembly of nanoparticles and this is responsible for the formation of the mesophase. On the other hand samples synthesized at higher temperature did not show this mesophase as the particle growth predominates at higher temperature leading to large zinc stannate nanoparticles. The wide-angle X-ray diffraction patterns of MZS-1 and MZS-2; two zinc stannate samples synthesized at different temperatures are shown in Figure 2. These PXRD patterns revealed that the material MZS-1 prepared at 348 K is made up of purely face-centered cubic perovskite $ZnSnO_3$ phase (JCPDS No.11-0274), whereas the sample MZS-2, prepared at comparatively higher temperature (448 K) is made up of face-centered cubic Zn_2SnO_4 crystallites (JCPDS No.00-024-1470).[28] Further, increasing the hydrothermal synthesis temperature causes perovskite $ZnSnO_3$ phase to convert into Zn_2SnO_4 and at 423 K both phases ($ZnSnO_3$ and Zn_2SnO_4) are present simultaneously. Below this temperature no Zn_2SnO_4 phase is observed; at 348, 373 and 393 K only pure face-centered cubic perovskite phase of $ZnSnO_3$ has been observed and this has been confirmed from the wide angle PXRD pattern of the materials. This is observed from the electron microscopic analysis also (see below). The X-ray diffraction peaks of samples have been compared with the JCPDS files of pure SnO_2 and ZnO nanomaterials. Absence of any X-ray diffraction peaks from these probable impurity phases suggested that both zinc stannate nanomaterials synthesized through salicylate templating pathway are highly stable and pure phases of the corresponding nanocrystallites.

Electron microscopic analysis:

The representative TEM images of mesoporous zinc stannate nanomaterials (MZS-1 and MZS-2) are shown in Figure 3. The HR TEM analysis of MZS-1 revealed that the material is composed of very tiny spherical nanoparticles of dimension *ca.* 1-2 nm (Figure 3b) and the white spots throughout the specimens of MZS-1 having average dimensions of *ca.* 1.9 - 2.7 nm (Figure 3a) is quite clear. These self-aggregated nanoparticles could be responsible for these interparticle voids and mesopores. The crystal structure of the mixed oxide depend on the hydrothermal temperature; at 348 K the crystal phase of the material has been designated as $ZnSnO_3$ with spherical morphology, at 423 K the material is composed of a mixture of spherical $ZnSnO_3$ and cubic Zn_2SnO_4 nanoparticles (Figure 3c) and finally at 453 K the pure Zn_2SnO_4 cubic phase has been observed. The HR TEM analysis of MZS-2 has been shown in Figure 3d. The material is composed of cubic crystalline nanoparticles with clear crystal edges of dimension 17-20 nm. (Figure 3e) The (111) lattice plane of Zn_2SnO_4 material is quite prominent in the TEM image. (Figure 3e) With increasing the particle size of the materials the tendency of self-aggregation decreases gradually, which is observable from this electron microscopic analysis of the material. The lattice fringes in the HR TEM image of the material MZS-2 suggest high crystallinity of the material. The distance between two crystal planes (Figure 3f) is quite good agreement with the *d* spacing of (111) crystal plane of cubic crystal structure with unit cell parameter *a*= 8.65 Å (JCPDS no: 241470). The corresponding FFT pattern of the MZS-2 material has been shown in Figure 4. Thus, while keeping the molar ratio of Zn/Sn constant in the synthesis gel it would be possible to achieve temperature induced crystal phase transformation in our newly developed zinc stannate synthesis pathway in the presence of sodium salicylate as the capping agent.

Porosity and Surface Area Analysis:

The Brunauer-Emmett-Tellller (BET) surface area and porosity of the mesoporous materials are estimated from the N_2 adsorption/desorption isotherms of the samples at 77 K. The adsorption/desorption isotherms for the samples MZS-1 and MZS-2 are shown in Figure 5A-B. The BET surface area of the sample MZS-1 is 117 m^2g^{-1} and the isotherm can be classified as typical type I having supermicroporosity along with mesoporosity. The BET surface area for the sample MZS-2 is 60 m^2g^{-1} and this isotherm is typical type IV with an H3 type hysteresis loop which is characteristic for mesoporous materials.[29] Their respective pore volumes are 0.0692 and 0.1404 ccg^{-1}. Corresponding pore size distribution of these samples estimated by employing the non-local density functional theory (NLDFT)[30] model is shown in the insets of Figure 5. Estimated pore dimension for the sample MZS-1 is 1.95 and 2.7 nm, suggesting that the material contains the pore in the supermicropore to mesopore region. On the other hand the average pore dimension for the sample MZS-2 varies from 5.6 to 6.9 nm. The *t*-method micropore analysis revealed the fact that MZS-1 contains the internal micropore area 96 m^2g^{-1} with micropore volume 0.0432 ccg^{-1} together with considerable interparticle mesopores.[31]

Thermal stability of zinc stannate mesophases:

The thermal stability of zinc stannate nanoparticles has been estimated from the TG-DTA profile of the samples under air flow with a heating rate of 10 $^oC\ min^{-1}$. The TG-DTA profile of MZS-1 is shown in the Figure 6. The TG-DTA plot shows three distinct weight losses. The first 10.20 wt% endothermic weight loss up to 464 K could be attributed to the loss of surface adsorbed water molecules along with partially burning of organic moieties in the self-assembled porous architecture. Further, 9.83 wt% weight loss with maxima at 641 K is assigned to the complete removal of organic moieties from the zinc stannate mesostructure. This is followed by a sharp exothermic peak corresponding to the internal phase transformation from the crystalline

$ZnSnO_3$ to amorphous nonporous material. The third weight loss at 964 K is attributed to the further phase transformation from amorphous material to mixture of Zn_2SnO_4 and SnO_2 phases. On the other hand the crystal phase of the sample MZS-2 is stable above 1000 K after heat treatment in air. These TGA results indicate that Zn_2SnO_4 is thermally more stable than $ZnSnO_3$.[32]

UV-visible spectra and Band Gaps of the nanomaterials:

The optical property of the zinc stannate nanomaterials is studied through the UV-visible diffuse reflectance spectroscopy. The UV-visible reflectance spectra of the as-synthesized porous samples MZS-1 and -2 are shown in Figures 7 and 8, respectively. MZS-1 shows absorption maxima at 314 nm and it is extended up to 398 nm, whereas MZS-2 shows absorption maxima at 260 nm and it is extended up to 399 nm. In both cases presence of extended absorption tails suggested the chemical binding of the salicylate molecules at the zinc stannate surface. The band gap energies of as-synthesized MZS-1 is 3.41 eV, whereas that of template-free MZS-2 is 3.27 eV. The band gap energy of as-synthesized MZS-2 is 3.59 eV. After heat treatment on Zn_2SnO_4 the absorption maxima is considerably red shifted to 292 nm and the corresponding band gap energy is 3.27 eV due to the incorporation of excess Zn into the zinc stannate nanocrystals.[28,33] The reported band gap energy for $ZnSnO_3$ is little high (3.9 eV).[34] Thus, in order to enhance its visible light induced photocatalic activity, we have introduced a π-conjugated system (salicylate molecules), which could cap the nanoparticles and thus can reduce the energy gap between HOMO and LUMO in MZS-1/2 composites compared to bulk zinc stannate. This is reflected in the corresponding UV-Vis reflectance spectrum and respective decrease in band gap energy.[35]

Temperature induced phase transformation:

The temperature is a crucial parameter for the hydrothermal synthesis of different nanostructured materials.[36] Here we have varied the synthesis temperature to get the most stable zinc stannate mesostructured materials with good surface area. The reactions are carried out at 348, 373, 393, 423 and 448 K, while other synthetic parameters are kept unchanged. When the synthesis temperatures are relatively low at 348-393 K pure $ZnSnO_3$ phase is formed, as the synthesis temperature is increased to 423 K the mixture of both phases ($ZnSnO_3$ and Zn_2SnO_4) have been observed. At further higher temperature 448 K, pure Zn_2SnO_4 has been formed exclusively. This result suggested that with the increasing the synthesis temperature $ZnSnO_3$ phase transform into Zn_2SnO_4 phase and particle size also is increased from 1-2 nm to 17-20 nm.[37] In this process first a rapid mixing of metal salt led to the formation of colloid particles which is immediately appeared in solution. This is due to the complex formation of $ZnSn(OH)_6$ which is insoluble in water, and excess Zn^{2+} react with OH^- and produce $Zn(OH)_4^{2-}$ phase, which is soluble in water. During the hydrothermal condition, when temperature is low (348, 373, 393 K) the $ZnSn(OH)_6$ formed as an unstable intermediate is transformed in to crystallites nanoparticles of $ZnSnO_3$ phase and excess Zn^{2+} could washout from the gel in form of $Zn(OH)_4^{2-}$ during the filtration after reaction. When the hydrothermal temperature increase up to 423 K some nuclei of $ZnSn(OH)_6$ could react with the $Zn(OH)_4^{2-}$, form Zn_2SnO_4 and some nuclei of $ZnSn(OH)_6$ direct transformed in $ZnSnO_3$ nanocrystals. At 448 K all nuclei of $ZnSn(OH)_6$ react with $Zn(OH)_4^{2-}$, to form pure Zn_2SnO_4 phase.[38] SDA molecule sodium salicylate plays very crucial role for the formation of mesophases and porosity. Zinc stannate nanoparticles bear considerable positive charge at their surface so that they can interact with the negatively charged carboxylate groups of sodium salicylate molecules via electrostatic interaction. In the ligated

salicylate moieties hydrogen bonding and hydrophobic interactions occurs due to the presence of ortho phenolic –OH group in the sodium salicylate and these interactions help to form supramolecular assembly under synthesis condition (Scheme 2).[39] Synthesis temperature also plays crucial role to stabilize the organized self-assembled mesophase. Low synthesis temperature is more favorable to form organized self-assembly leading to a mesophase rather than at higher temperature. Probably due to this reason only at 348 K self-assembled zinc stannate mesostructure has been observed.[40]

Photocatalytic degradation of Rhodamine B:

The photocatalytic activity of the as-prepared material MZS-1 and MZS-2 for the degradation of Rhodamine B dye (RhB) under UV and visible light irradiation have been shown in Figure 9. Rhodamine B shows strongest absorption peak at 553 nm. The band gap and surface area of the semiconductor nanocrystal plays an important role in the degradation of organic dye molecule.[41] The dye degradation capacity of the material MZS-1 ($ZnSnO_3$) and MZS-2 (Zn_2SnO_4) for 5 mgL^{-1} RhB solution under UV light irradiation have been shown in Figure 9a and 9b and the corresponding result for MZS-2 (Zn_2SnO_4) with same concentration of dye solution under visible light has been shown in Figure 9c. The lower band gap of the materials is responsible for high photocatalytic activity under visible/UV lights. Due to this reason the material MZS-2 (3.27 eV) shows better photocatalytic property than the material MZS-1 (3.41 eV) under UV as well as visible light irradiation. The surface area and mesoporous architecture enhances the opportunity for the organic dyes to penetrate into the inside the pores and come in direct contact with the nanoparticle surface and thus more dye molecule can degrades.[42] In the case of visible light driven photocatalytic degradation of dye by the binary semiconducting metal oxide nanocrystals the dye sensitization mechanism has been considered to be the most crucial

(Scheme 3a).[43] As the injection of electron from the conduction band of dye molecule to the LUMO of semiconductor material is prime criteria for the dye degradation under visible light, direct contact between the organic dye molecule and the semiconductor material is very essential.[44] So inorganic semiconductor porous nanomaterials with high surface area is responsible for higher dye degradation rate under visible light.[45] In our case, the surface area of the MZS-1 is higher than MZS-2 but the material MZS-1 bears salicylate molecules organic moiety. Hence due to the more energetically favorably π-π stacking interaction, the chromophore molecules get absorbed in higher amount in the organic part of the MZS-1 material; so the contact between the active catalytic site and dye molecule significantly decreases. Thus, the electron flow under visible light through diffusion is hampered in case of MZS-1 due to the insignificant interaction between two organic scaffold molecules (SDA) and Rhodamine B.[46] Now in case of MZS-2, lower energy gap between HOMO and LUMO than MZS-1 along with absence of any aromatic conjugated system in the porous framework facilitate its fast catalytic pathway. Further, the photocatalytic activity over a solid support could change dramatically because the aggregation of the nanoparticles normally limits the diffusion process.[47] Thus, the enhancement in the photocatalytic activity of Zn_2SnO_4 over that of $ZnSnO_3$ can also be explained due to the faster diffusion of reactants and products during the photodegradation process.

On the other hand the scenario for the dye degradation in the presence of UV light is little different. In the presence of the UV light dye degradation takes place through the generation of the electron–hole pair, Upon UV light irradiation, electrons (e^-) in the valence band of semiconductor are excited to the conduction band with the simultaneous generation of holes (h^+) in the valence band. These electron-hole pair is responsible for dye degradation in UV light (Scheme 3b).[48] Our experimental results show that the photocatalytic efficiency of MZS-1 is

quite stumpy than MZS-2 under UV light also. There are three probable reasons behind low catalytic activity of MZS-1 over MZS-2 under UV light irradiation: (i) The bandgap of the material MZS-1 is higher than Material MZS-2, (ii) the surface of material, MZS-1 is coated by salicylate moieties so the number of photon interact with the inorganic framework decreases hugely; but in case of MZS-2, there is no chance of such type of phenomenon. So in case of MZS-2; the inorganic semicondactor material enjoy the maximum photon interaction[46] and (iii) during dye degradation holes is generated in photocatalyst, these photogenerated holes are trapped by hydroxyl groups ($^{-}$OH) at the semiconductor to yield hydroxyl radicals ($^{\bullet}$OH) or directly trapped by organic pollutions to further oxidize organic pollutants.[49] But in the case of MZS-1 material these holes is stabilized by surface salicylate moieties, so the rate of formation of ($^{\bullet}$OH) decrease tremendously, as a consequence relatively lower amount of dye degrades. We have tried to detect the reactive hydroxyl free radicals through EPR analysis at room temperature (298 K) and liquid N_2 temperature (77 K) but we did not get any fruitful results. This could be due to the very short life-time of hydroxyl radical in aqueous medium.[50] Now the obvious question arises why we are comparing the photodegradation property of two materials prepared by different methods? Actually our aim in this research work was to synthesize the porous mixed oxide with Zn and Sn with different crystal structure and morphology by tuning the reaction parameters and compare their photocatalytic activities. The textural features of the two mixed oxides ($ZnSnO_3$ and Zn_2SnO_4) are completely different. At higher temperature (> 573 K) the crystal structure of $ZnSnO_3$ completely collapsed.[32] Thus, retention of crystal structure after the removal of organics from the framework of MZS-1 could not be achieved at higher temperature. Hence, from the porous $ZnSnO_3$ we could not remove the organics (even by calcinations at inert atmosphere) to get the completely inorganic porous framework. So we are compelled to compare

the photocatalytic activity of two materials prepared at different process. The observed photocatalytic activities for both MZS-1 and MZS-2 with higher concentrations of dye (10 mgL^{-1} and 20 mgL^{-1}) were little lower than that of 5 mgL^{-1} dye solution. The chemical oxygen demand (COD) test is used to measure the amounts of required oxygen for the degradation of organic matter to CO_2 and H_2O in waste water. The reduction in COD values of the treated dye solution indicates the mineralization of dye molecules. Here we have calculated the initial and final COD of the dye solution (10 mg/lit) to confirm the catalytic activity of the mesoporous mixed oxide (MZS-2) by previously reported procedures and photodegradation efficiency of the material (MZS-2). The calculated initial and final COD (after dye degradation under UV light in presence of MZS-2) of the 10 mg/lit RhB solution is 5.04 mg/L and 0.16 mg/L respectively.

Recyclability of the catalyst:

We have used MZS-2 for three consecutive cycles in the degradation of RhB to confirm the reusability and heterogeneous nature of the photocatalyst (Figure 9d). The catalyst was recovered from the reaction mixture by filtration and washed two times with ethanol to remove surface absorbed dye molecule. Before performing the photoreaction again, the catalyst was dried at 298 K for 12 h and reused. From the Figure 9d, it is quite clear that the photocatalytic activity of the material do not hampered much after three conjugative catalytic cycles suggesting our porous zinc stannate nanocrystals can be utilized efficiently for the photodegradation reactions.

Kinetic study:

Here we have calculated the photocatalytic degradation efficiency of self-assembled mesoporous zinc stannate nanoparticles by Beer–Lambert law. The concentration of RhB dye molecule in aqueous solution is linearly proportional to the intensity of maxima (553 nm)

absorption peak, and hence the degradation efficiency of RhB can be calculated using the following expression:

$$\text{RhB degradation (\%)} = (C_0 - C)/C_0 \text{ X100}$$

Where C_0 is the initial concentration of aq. dye solution and C is the concentration of dye after irradiation at any time t, respectively. The photocatalytic efficiency of different catalysts (MZS-1 and MZS-2) for different concentration (20 mg L^{-1}, 10 mg L^{-1}, and 5 mg L^{-1}) of dye solution under UV-vis light has been shown in Table 1. The corresponding kinetic plots have been shown in Figure 10. In the absence of the photocatalyst and light the rate of dye degradation is very slow (negligible). The rate of dye degradation is very fast on irradiation of UV light rather than visible light. For low concentration (5 mgL^{-1}) of dye the material MZS-2 takes only 100 min for the complete degradation. The beauty lies behind the fast catalytic activity of the material without use of any peroxide. It takes only 120 min and 140 min for to degrade 10 mgL^{-1} and 20 mgL^{-1} of the dye molecule in aqueous medium. From the kinetic plots (Figure 10), we have calculated the pseudo first ordered rate constants for the dye degradation by employing the following equation:

$$\ln C = \ln C_0 - kt$$

Where t is reaction time, k is the rate constant; C_0 and C are the dye concentrations initially and after time t, respectively.[50] The corresponding rate constants (k) values for the material MZS-1 and MZS-2 has been given in Table 1, which suggests Zn_2SnO_4 nanocrystals has higher photocatalytic activity over that of $ZnSnO_3$.

Conclusions

Fabrication of binary semiconducting metal oxide nanocrystals with porosity and high surface area has been achieved through a novel synthesis strategy reported here. Self-assembled tiny zinc stannate nanocrystals having controlled phases of $ZnSnO_3$ (MZS-1) or Zn_2SnO_4 (MZS-2) with particle dimensions of *ca.* 1-2 nm for MZS-1 and 17-20 nm for MZS-2 have been reported for first time via salicylate templating method. Both binary semiconducting metal oxide nanocrystals Zn_2SnO_4 and $ZnSnO_3$ showed high photocatalytic activity in the photodegradation of Rhodamine B under visible and UV light illumination. This result suggested that the mesoporous zinc stannate nanocrystals can be utilized efficiently for the photodegradation reactions. Our objective is to synthesize the zinc stannate nanocrystals with different crystal structures and morphological diversity along with mesoscopic void space and compare their photocatalytic property for the degradation of Rhodamine B under UV/visible light. The materials are low-cost, stable, nontoxic and easily reproducible that can be efficiently used for waste water treatment in dye industry. As these inorganic nanocrystals are insoluble in any organic solvent or aqueous media, these photo-catalysts can be easily recovered after use. Further, since the degradation of dyes using UV light is not a green approach; the efficient visible-light-driven photocatalysis over porous MZS-2 could largely utilize to remove the organic pollutants from waste water. Due to the high thermal stability together with low band gap these ultra-small zinc stannate nanocrystals may find potential utility in other optoelectronics applications in future.

Acknowledgements. VK and AKP thank CSIR, New Delhi for their respective junior and senior research fellowships. AB wishes to thank DST, New Delhi for instrumental supports through the DST Unit on Nanoscience and SERB project grants.

References and Notes:

1 (a) J. H. Fendler, *Chem. Mater*., 1996, **8**, 1616; (b) S. M. Lee, S. N. Cho and J. Cheon, *Adv. Mater*., 2003, **15**, 441; (c) F. X. Redl, K. S. Cho, C. B. Murray and S. O'Brien, *Nature*, 2003, **423**, 968.

2 (a) G. Katsukis, J. Malig, C. Schulz-Drost, S. Leubner, N. Jux and D. M. Guldi, *ACS Nano*, 2012, **6**, 1915; (b) W. D. Shi, S. Y. Song and H. J. Zhang, *Chem. Soc. Rev*., 2013, **42**, 5714.

3 (a) W. U. Huynh, J. J. Dittmer and A. P. Alivisatos, Science, 2002, **295**, 2425; (b) N. Tetreault and M. Grätzel, *Energy Environ. Sci*., 2012, **5**, 8506.

4 I. L. Medintz, A. R. Clapp, H. Mattoussi, E. R. Goldman, B. Fisher and J. M. Mauro, *Nature Mater*., 2003, **2**, 630.

5 R. Marega, F. D. Leo, F. Pineux, J. Sgrignani, A. Magistrato, A. D. Naik, Y. Garcia, L. Flamant, C. Michiels and D. Bonifazi, *Adv. Funct. Mater.*, 2013, **23**, 3173.

6. G. A. Seisenbaeva, M. P. Moloney, R. Tekoriute, A. H. Dessources, J. M. Nedelec, Y. K. Gunko and V. G. Kessler, *Langmuir*, 2010, **26**, 9809; (b) M. Colilla, M. Manzano, I. I. Barba, M. V. Regi, C Boissiere and C. Sanchez, *Chem. Mater.*, 2010, **22**, 1821.

7 J. G. Yu, Y. R. Su and B. Cheng, *Adv. Funct. Mater*., 2007, **17**, 1984.

8 B. H. Wu, C. Y. Guo, N. F. Zheng, Z. X. Xie and G. D. Stucky, *J. Am. Chem. Soc*., 2008, **130**, 17563.

9 N. V. Long, M. Ohtaki, M. Uchida, R. Jalem, H. Hirata, N. D. Chien and M. Nogami, *J. Colloid Interface Sci.*, 2011, **359**, 339.

10 R. Ramakrishnan, J. D. Sudha and V. L. Reena, *RSC Adv.,* **2012**, *2*, 6228-6236.

11 A. Corma, P. Atienzar, H. Garcia and J. –Y. Chane-Ching, *Nature,* 2004, **3**, 394.

12 S. K. Das, M. K. Bhunia, A. K. Sinha and A. Bhaumik, *J. Phys. Chem. C,* 2009, **113**, 8918.

13 (a) J. Ba, J. Polleux, M. Antonietti and M. Niederberger, *Adv. Mater.,* 2005, **17**, 2509; (b) C. Aprile, L. Teruel, M. Alvaro and H. Garcia, *J. Am. Chem. Soc.,* 2009, **131**, 1342.

14 J. P. Wang, T. Xia, C. L. Wu, J. Feng, F. C. Meng, Z. Shi and J. Meng, *RSC Adv.,* **2012**, *2*, 4220-4227.

15 C. Pacholski, A. Kornowski and H. Weller, *Angew. Chem. Int. Ed*., 2002, **41**, 1188.

16 (a) Y. J. Chen, L. Yu, Q. Li, Y. Wu, Q. H. Li and T. H. Wang, *Nanotechnol*., 2012, **23**, 415501; (b) Y. J. Chen, B. H. Qu, L. Mei, D. N. Lei, L. B. Chen, Q. H. Li, T. H. Wang, *J. Mater. Chem*., 2012, **22**, 25373; (c) Z. F. Tian, C. H. Liang, J. Liu, H. M. Zhang and L. D. Zhang, *J. Mater. Chem*., 2012, **22**, 17210; (d) Y. Zeng, X. G. Wang and W. T. Zheng, *J. Nanosci. Nanotechnol*. 2013, **13**, 1286.

17 (a) Y. Zeng, K. Zhang, X. L. Wang, Y. M. Sui, B. Zou, W. T. Zheng and G. T. Zou, *Sensor Actuator B: Chem*. 2011, **159**, 245; (b) X. G. Han, X. W. Cao, L. Li and C. Wang, *Sensor Actuator B: Chem*. 2013, **185**, 383.

18 H. T. Fan, Y. Zeng, X. J. Xu, N. Lv and T. Zhang, *Sensor Actuator B: Chem*. 2011, **153**, 170.

19 E. Obert, M. Bellot, L. Bouteiller, F. Andrioletti, C. Lehen-Ferrenbach and F. Boué, *J. Am. Chem. Soc.,* 2007, **129**, 15601.

20 J. Jin, T. Iyoda, C. Cao, Y. Song, L. Jiang, T. Li and D. Zhu, *Angew, Chem., Int. Ed.,* 2001, **40**, 2135.

21 Y. Zhou and M. Antonietti, *J. Am. Chem. Soc.,* 2003, **125**, 14960.

22 G. Mialon, M. Gohin, T. Gacoin and J. P. Boilot, *ACS Nano*, 2008, **2**, 2505.

23 C. Klingshirn, *ChemPhysChem*, 2007, **8**, 782.

24 M. A. Lazar and W. A. Daoud, *RSC Adv*., 2013, **3**, 4130

25 C. A. Martinez-Huitle and E. Brillas, *Appl. Catal. B: Environ*., 2009, **87**, 105.

26 I. Paramasivam, H. Jha, N. Liu and P. Schmuki, *Small*, 2012, **8**, 3073.

27 Y. Zhou and M. Antonietti, *J. Am. Chem. Soc.*, 2003, **125**, 14960.

28 (a) M. Miyauchi, Z. Liu, Z. G. Zhao, S. Anandan and K. Hara, *Chem. Commun.*, 2010, 46, 1529; (b) Z. Wang, J. Liu, F. Wang, S. Chen, H. Luo, and X. Yu, *J. Phys. Chem. C.,* 2010, **114**, 13577.

29 (a) D. Chandra, B. K. Jena, C. R. Raj and A. Bhaumik, *Chem. Mater.,* 2007**, 19***,* 6290; (b) M. Pramanik, M. Nandi, H. Uyama and A. Bhaumik, *Catal. Sci. Technol.,* 2012, **2**, 613.

30 P. I. Ravikovitch and A. V. Neimark*, J. Phys. Chem. B,* 2001**, 105**, 6817.

31 I. Tanahashi A. Yoshida and A. Nishino, *Carbon*, 1991, **29**, 1033.

32 (a) S. H. Wei and S. B. Zhang, *Phys. Rev. B*, 2001, **63**, 045112; (b) D. Segev and S. H. Wei, *Phys. Rev. B,* 2005, **71**, 125129.

33 M. A. A. Aviles and Y. Wu, *J. Am. Chem. Soc.,* 2009, **131**, 3216.

34 Z. Tian, C. Liang, J. Liu, H. Zhang and L. Zhang, *J. Mater. Chem.,* 2012, **22**, 17210.

35 A. K. Patra, A. Dutta, A. Bhaumik, *J. Hazard. Mater*., 2012, **201-202**, 170.

36 D. Zhao, Q. Huo, J. Feng, J. Kim, Y. Han and Galen D. Stucky, *Chem. Mater*., 1999, **11**, 2668.

37 Z. Wang, J. Liu, F. Wang, S. Chen, H. Luo and X. Yu, *J. Phys. Chem. C.,* 2010, **114**, 13577.

38 J. Zeng, M. Xin, K. W. Li, H. Wang, H. Yan and W. J. Zhang, *J. Phys. Chem. C.,* 2008, **112**, 4159.

39 A. K. Patra, S. K. Das and A. Bhaumik, *J. Mater. Chem.*, 2011, **21**, 3925.

40 (a) H. Colfen and S. Mann, *Angew. Chem. Int. Ed*., 2003, **42**, 2350; (b) X. M. Liu, G. Q. Lu and Z. F. Yan, *J. Phys. Chem. B,* 2004, **108**, 15523.

41 (a) S. K. Das, M. K. Bhunia and A. Bhaumik, *Dalton Trans.*, 2010, **39**, 4382; (b) M. Srinivasan and T.White, *Environ. Sci. Technol*. 2007, **41**, 4405.

42 C. Fang, B. Geng, J. Liu and F. Zhan, *Chem. Commun.,* 2009, 2350.

43 S. Rehman, R. Ullah, A. M. Butt and N. D. Gohar, *J. Hazard. Mater.,* 2009, **170**, 560.

44 (a) Z. Zhai, C. Hu, X. Yang, L. Zhang, C. Liu, Y. Fan and W. Hou, *J. Mater. Chem*., 2012, **22**, 19122; (b) M. Pramanik, A. K. Patra and A. Bhaumik, *Dalton Trans*., 2013, **42**, 5140.

45 Z. Frontistis, D. F. Kassinos, D. Mantzavinosa and N. P. Xekoukoulotakis, *J. Chem. Technol. Biotechnol.* 2012, **87**, 1051; (b) N. Pal, M. Paul, A. Bera, D. Basak and A. Bhaumik, *Anal. Chim. Acta*, 2010, **674**, 96–101.

46 H. Liu, X. Dong, G. Li, X. Su and Z. Zhu, *Appl. Surf. Sci*., 2013,**271**, 276.

47 (a) C. Wang and W. B. Lin *J. Am. Chem. Soc*., 2011, **133**, 4232; (b) M. M. Wanderley, C. Wang, C. –D. Wu and W. B. Lin, *J. Am. Chem. Soc*., 2012, **134**, 9050.

48 (a) S. K. Kansal, M. Singh and D. Sud, *J. Hazard. Mater.,* 2007, **141**, 581; (b) S. Ma, R. Li, C. Lv, W. Xu, X. Gou, *J. Hazard. Mater.,* 2011, **192**, 730.

49 (a) M. J. Kim, S. H. Park and Y. D. Huh, *Bull. Korean Chem. Soc*., 2011, **32**, 1757; E. L. Foletto, J. M. Simoes, M. A. Mazutti, S. L. Jahn, E. I. Muller, L. S. F. Pereira, E. M. de Moraes Flores, *Ceramics Int*., 2013, **39**, 4569.

50 R. G. Zepp, *Envlron. Sci. Technol.*, 1992, **26**, 313.

51 (a) J. Yu, G. Dai, and B. Cheng, *J. Phys. Chem. C,* 2010, **114**, 19378; (b) M. Li, G. Huang, Y. Qiao, J. Wang, Z. Liu, X. Liu and Y. Mei, *Nanotechnol*.,, 2013, **24**, 305706; (c) R. Chauhan, A. Kumar, R. P. Chaudhary, *Spectrochimica Acta Part A: Mol. Biomol. Spect.*, 2013, **113**, 250.

Table 1. Photodegradation of RhB over MZS-1 and -2 in the presence of UV-vis light.

Catalyst[a]	Concentration of chromophore molecules (mg/L) [b]	Time (min)	Photodegradation efficiency (%)[c]	Rate constant k/min^{-1}	Light source[d]
MZS-2	5	100	98.6	0.040	UVL
MZS-2	10	120	98.4	0.032	UVL
MZS-2	20	140	97.3	0.026	UVL
MZS-2	5	180	90.3	0.012	VL
MZS-2	10	180	84.5	0.0096	VL
MZS-2	20	175	71.1	0.0068	VL
MZS-1	5	120	62	0.0078	UVL
MZS-1	10	120	49	0.0054	UVL
MZS-1	20	160	36	0.0036	UVL

[a] Catalyst used for the Photodegradation reaction = 50 mg.

[b] Here we have used Rhodamine B as the chromophore molecule.

[c] Percentage of dye degradation has been calculated from the UV-visible spectroscopy involving Beer - Lambert law.

[d] UVL = Ultra violet light, VL = Visible light

Figure captions

Figure 1. Small angle XRD patterns of as-synthesized material MZS-1.

Figure 2. Wide angle XRD patterns of as-synthesized material at different temperatures: 348 (MZS-1), 373, 393, 423 and 448 K (MZS-2, calcined).

Figure 3. HR TEM images of self-assembled zinc stannnate nanoparticles **(a**, **b**, **c**, **d** and **e)** and selected area electron diffraction (SAED) pattern for the material MZS-2 **(f).**

Figure 4. The FFT of the material MZS-2.

Figure 5. N_2 adsorption (●)-desorption (○) isotherms of the as-synthesized material MZS-1 (top) and MZS-2 (down) at 77 K. Corresponding NLDFT pore size distributions are shown in the inset.

Figure 6. TG-DTA profile of the as-synthesized material MZS-1

Figure 7. UV-Visible diffuse reflectance spectrum of MZS-1. Bandgap of the material is shown in inset.

Figure 8. UV-Visible diffuse reflectance spectrum for MZS-2. Bandgap of material is shown in inset.

Figure 9. Rhodamine B (5 mgL^{-1}) degradation by different photocatalyst MZS-1 (a) MZS-2 (b) under UV light and MZS-2 (c) under visible light and corresponding reusability curve (d) with MZS-2.

Figure 10. Kinetics of the photodecomposition of RhB over MZS-2 (A) and MZS-1 (B) under UV/visible light. WC: without catalyst; WOL: without light.

Scheme 1. Proposed chemical reactions during the synthesis of $ZnSnO_3$ and Zn_2SnO_4 nanoparticles.

Scheme 2. Role of synthesis temperatures on the particle morphology and self-assembled nanostructures of zinc stannate.

Scheme 3. Mechanistic pathways for the photodecomposition of RhB over mesoporous zinc stannate nanocrystals.

Figure 1 [Kumari, Patra and Bhaumik]

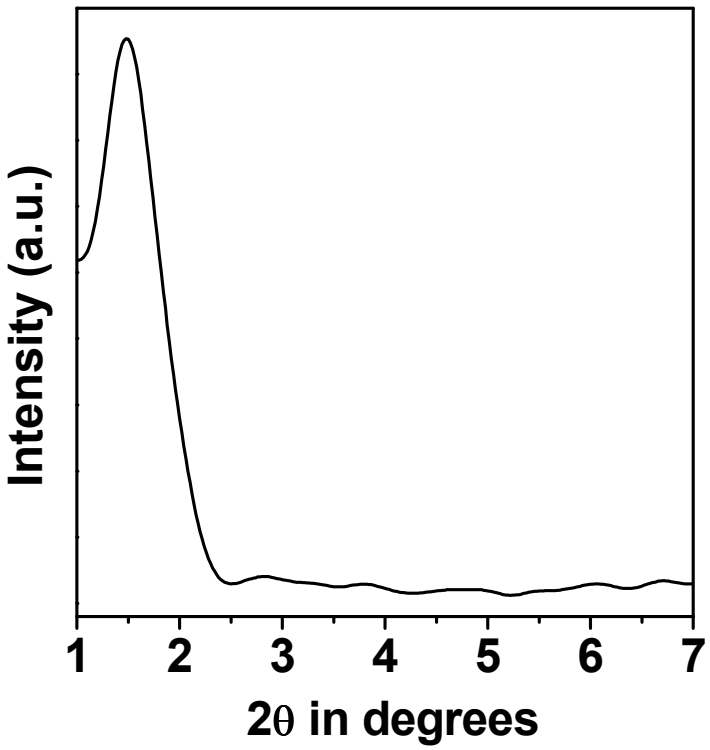

Figure 2 [Kumari, Patra and Bhaumik]

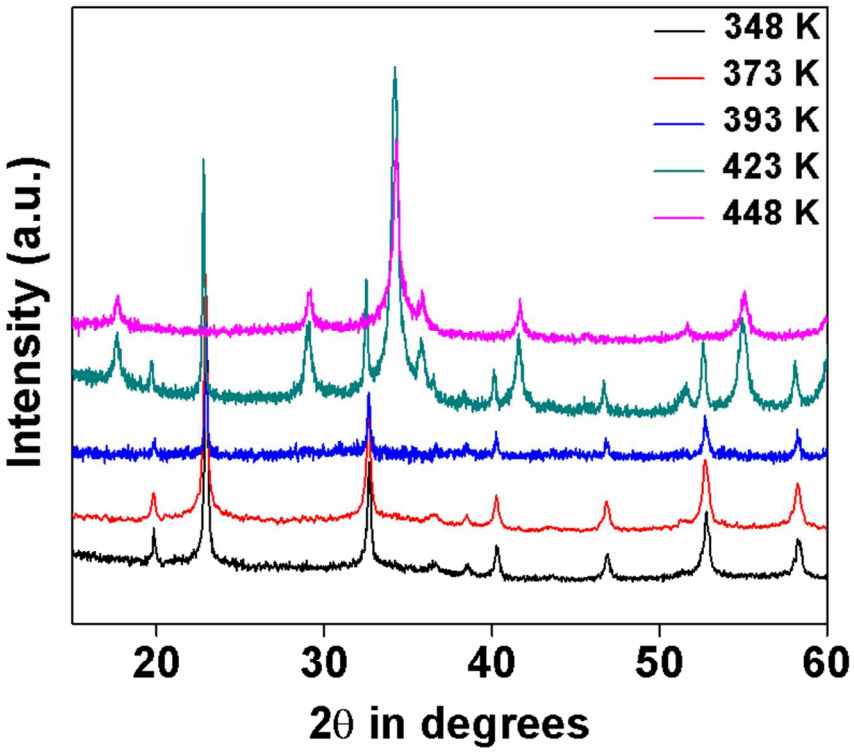

Figure 3 [Kumari, Patra and Bhaumik]

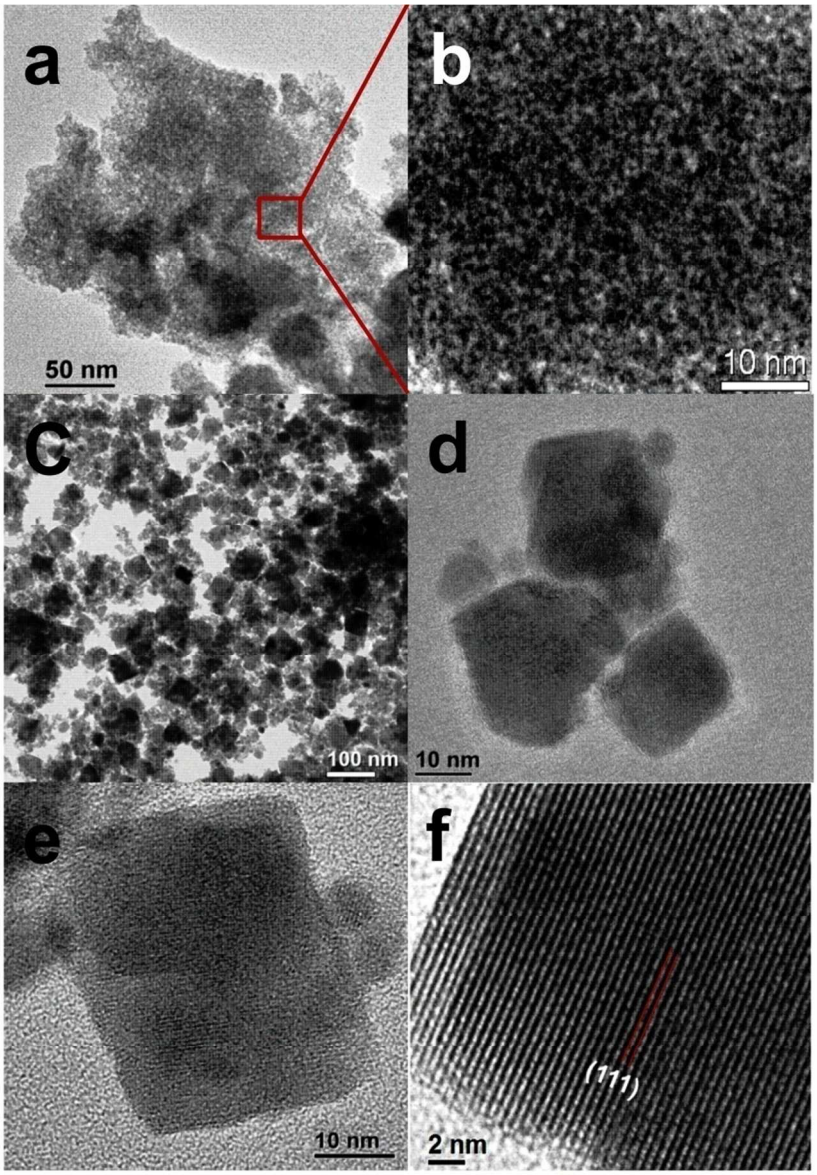

Figure 4 [Kumari, Patra and Bhaumik]

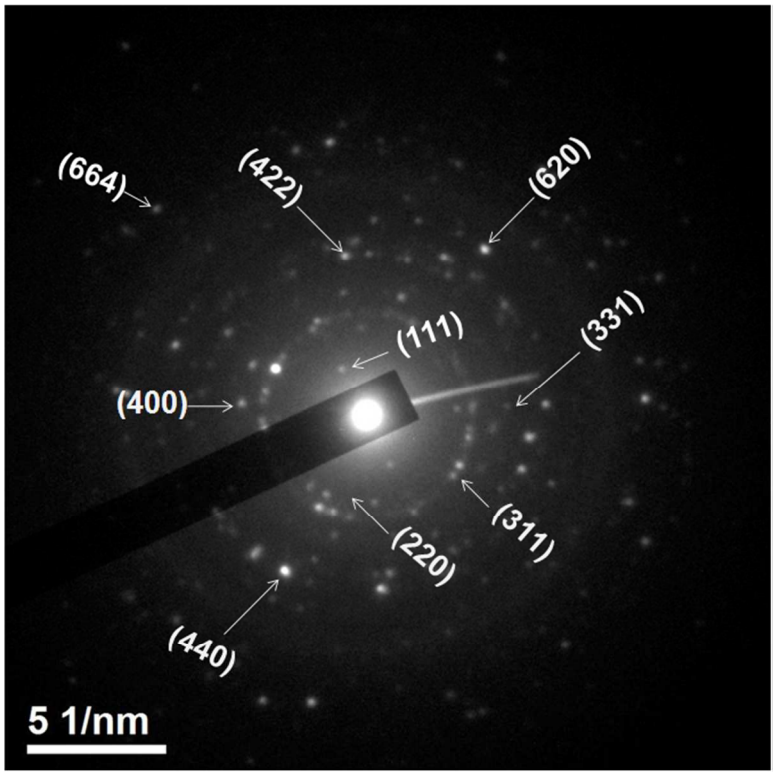

Figure 5 [Kumari, Patra and Bhaumik]

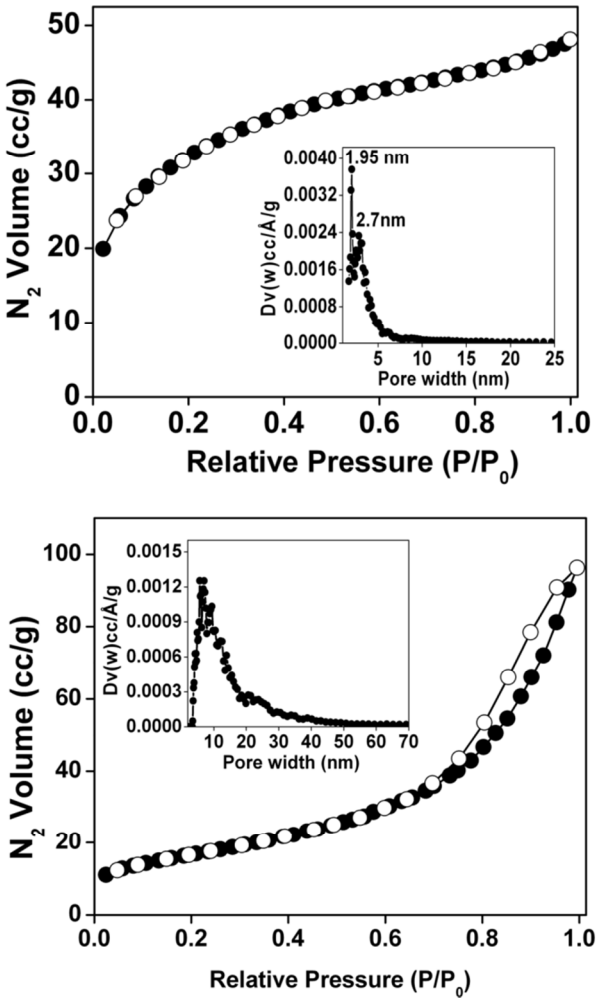

Figure 6 [Kumari, Patra and Bhaumik]

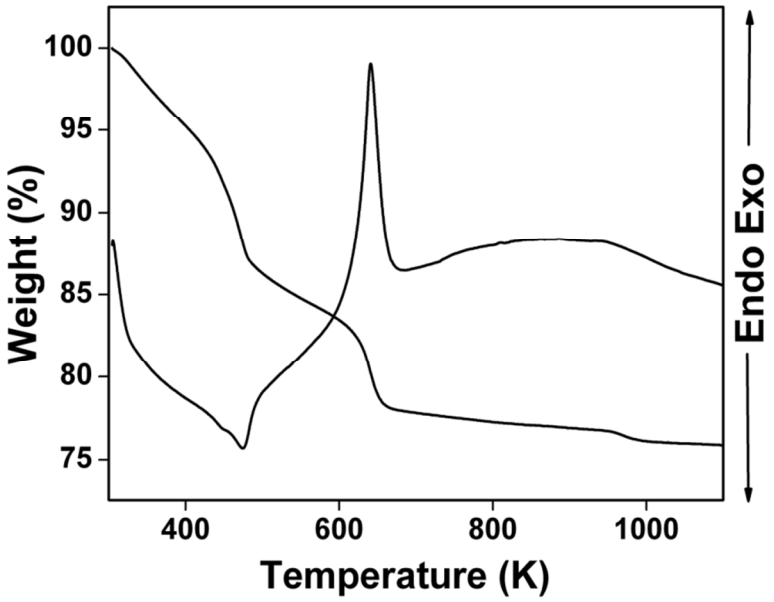

Figure 7 [Kumari, Patra and Bhaumik]

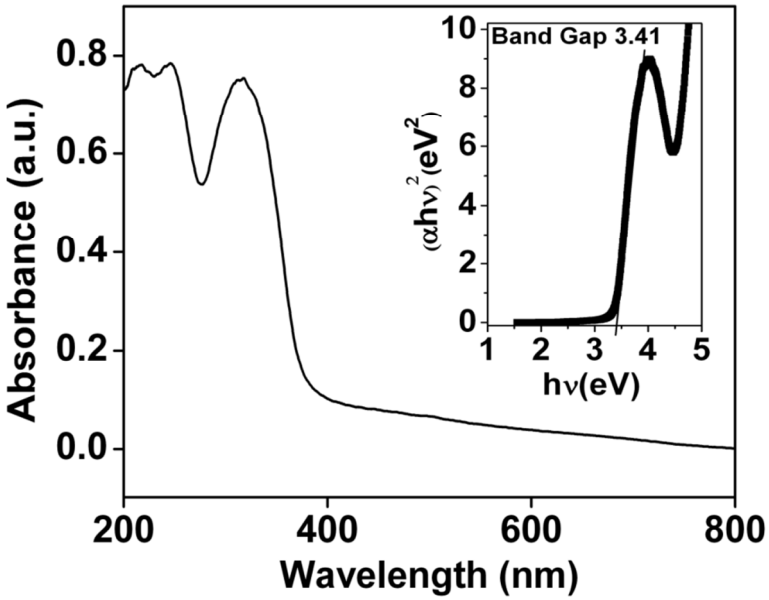

Figure 8 [Kumari, Patra and Bhaumik]

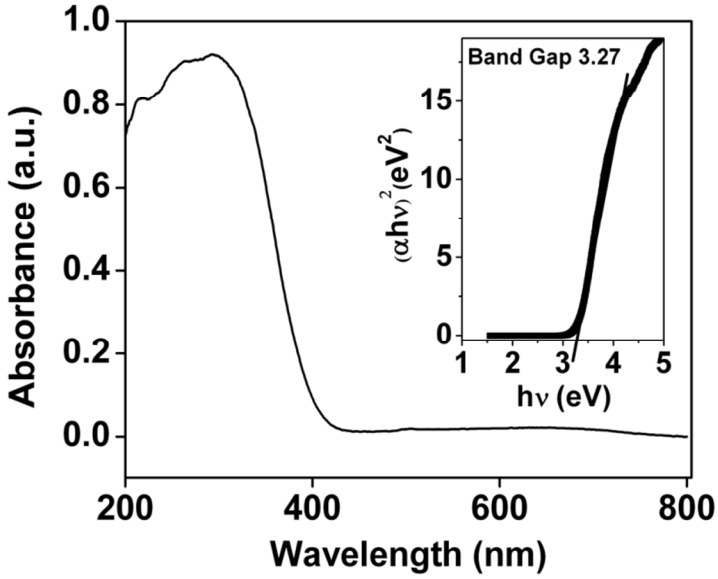

Figure 9 [Kumari, Patra and Bhaumik]

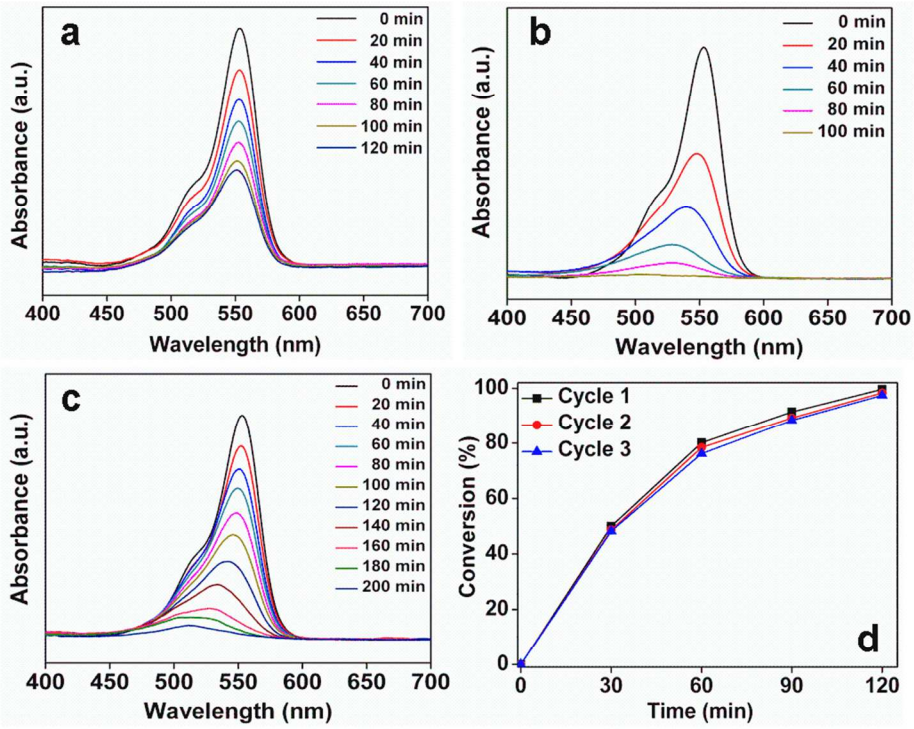

Figure 10 [Kumari, Patra and Bhaumik]

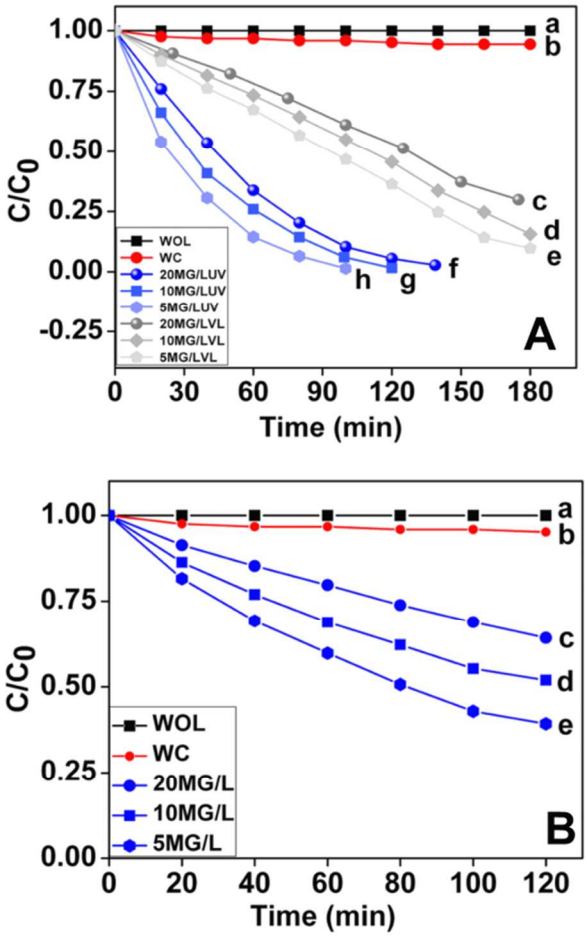

Scheme 1 [Kumari, Patra and Bhaumik]

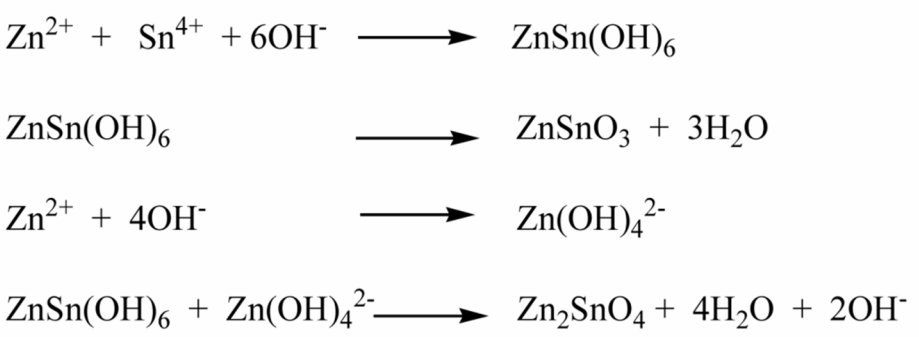

Scheme 2 [Kumari, Patra and Bhaumik]

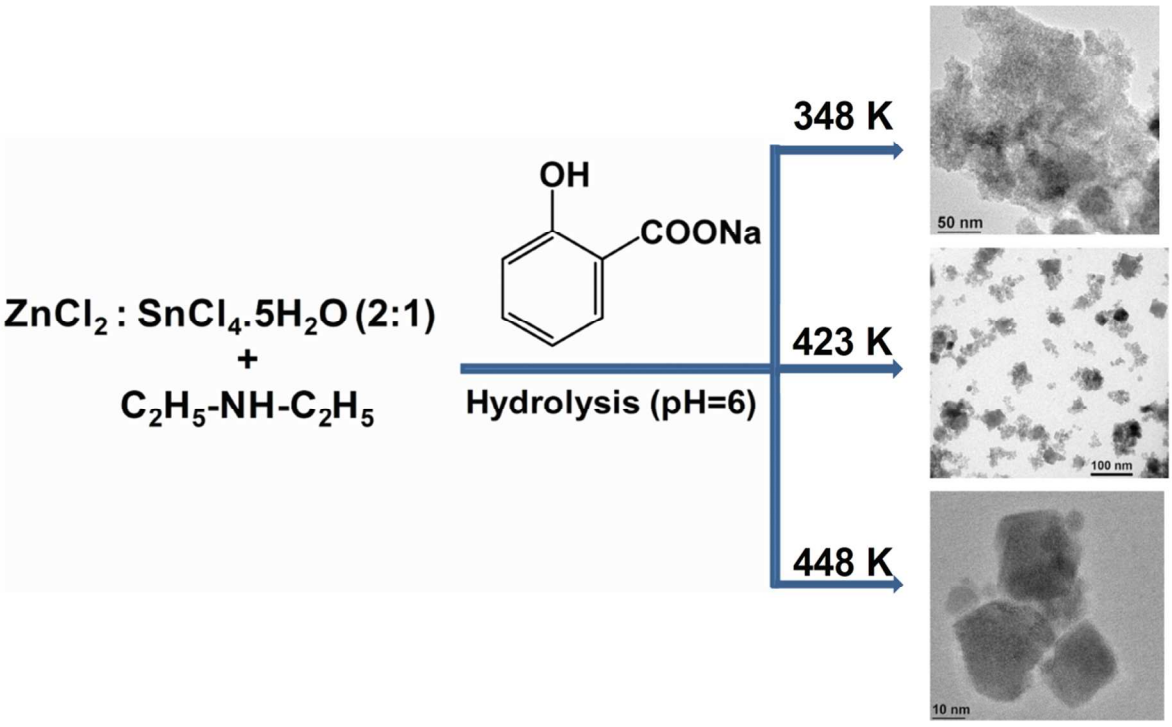

Scheme 3 [Kumari, Patra and Bhaumik]